Nanomechanical modulation cavities of localized surface plasmon resonance with elastic whispering-gallery modes

Z. Oumekloul, M. Moutaouekkil, Gaëtan Lévêque, Abdelkrim Talbi, A. Mir, Abdellatif Akjouj

Journal of Applied Physics

Nanomechanical modulation cavities of localized surface plasmon resonance with elastic whispering-gallery modes

Cite as: J. Appl. Phys. **127**, 023105 (2020); https://doi.org/10.1063/1.5111819
Submitted: 31 May 2019 • Accepted: 22 December 2019 • Published Online: 13 January 2020

Z. Oumekloul, M. Moutaouekkil, G. Lévêque, et al.

Journal of Applied Physics ARTICLE scitation.org/journal/jap

Nanomechanical modulation cavities of localized surface plasmon resonance with elastic whispering-gallery modes

Cite as: J. Appl. Phys. **127**, 023105 (2020); doi: 10.1063/1.5111819
Submitted: 31 May 2019 · Accepted: 22 December 2019 ·
Published Online: 13 January 2020

Z. Oumekloul,[1,2,a)] M. Moutaouekkil,[3] G. Lévêque,[2] A. Talbi,[3] A. Mir,[1] and A. Akjouj[2]

AFFILIATIONS

[1]Laboratory for the Study of Advanced Materials and Applications (LEM2A), Physics Department, Moulay Ismail University of Meknes, B.P. 11201, Zitoune, Meknes, Morocco
[2]Department of Physics, FST, Institute of Electronics, Microelectronics and Nanotechnology, CNRS–UMR 8520, University of Lille, Villeneuve d'Ascq 59652, France
[3]Institute of Electronics, Microelectronics and Nanotechnology, CNRS UMR 8520, LIA LEMAC-LICS, Centrale Lille, University of Lille, Lille F-59000, France

[a)]**Author to whom correspondence should be addressed:** z.oumekloul@edu.umi.ac.ma

ABSTRACT

The dispersion of mechanical vibration limits nano-optomechanical modulation. In this work, we propose an optomechanical modulation exploiting elastic local resonances, also called whispering-gallery modes (WGMs). We find that our structure supports two quadripolar and two hexapolar elastic WGMs, which are nondispersive to avoid losses where the displacement field is localized on the gold nanodisks (AuNDs). We numerically demonstrate that the coupling between localized surface plasmon resonance (LSPR) and WGMs are relative both to the symmetry displacement of the elastic modes and to the strong isolation of phononic modes in the AuNDs. The amplitude of the modulation is evaluated by computing the wavelength shift of dipolar LSPR under different deformations by four WGMs. A detailed comparison between the four WGMs allows us to determine the ones with more efficient coupling. Furthermore, this simultaneous confinement gives a large acousto-plasmonic coupling that can be used to design a new mechanical sensor with the plasmonic response as a potential application and innovation toward new acousto-plasmonic devices.

I. INTRODUCTION

Phonon modes supported by noble metal nanoparticles (NPs) have attracted particular attention since they interact with localized surface plasmon resonances (LSPRs), leading to a strong modulation of the plasmonic response.[1–7] Understanding this modulation is paramount for both fundamental and applied aspects. LSPRs are associated with the collective resonant oscillation of conduction electrons excited by an external electromagnetic field in metal NPs whose light confining properties make it possible to overcome the diffraction limit, which imposes the minimal dimensions of optical devices. Also, it should be noted that the resonance frequency depends on the shape and size of the NPs.[8–10] The manipulation and control of LSPR modes have led to the development of numerous applications in various fields such as biosensitivity,[11–16] surface Raman spectroscopy,[17–19] and solar cells.[20–23] Besides, NPs support elastic whispering-gallery modes (WGMs) that can have very high-quality factors,[24] with near-zero group velocities due to the local resonance mechanism, and frequencies up to terahertz.[25,26] The properties of these phononic modes are widely used in phononic crystals for filtering and detecting applications.[27–29] The significant excitation and confinement properties of LSPRs and WGMs depend on size, shape, and nanostructuring, which allows us to optimize plasmon-phonon interaction. Many experimental works have been conducted to study the acousto-plasmonic interactions either by Raman or pump-probe spectroscopies[30–32] on NPs with different geometries, allowing a wide range of light enhancement and resonance wavelength. The mechanical vibration alters the shape and the dielectric function of metal NPs, which can be used to design a mass detector to weigh molecules.[33]

Although the manipulation of the objects at the nanoscale presents technical difficulties, many experiments were carried out as early as the 1980s by very-low-frequency Raman scattering to highlight acousto-plasmonic coupling.[34] These oscillations not only change the shape of the NPs but also alter their dielectric constant in the crystal structure and will, therefore, slightly modulate their plasmonic properties. For example, Mrabti *et al.*[2] studied, numerically and theoretically, the acousto-plasmonic coupling of metal-insulator-metal (MIM) plasmon modes supported by metal film-particle systems. The nature of these modes (MIM) is very different from the localized modes supported by an isolated particle on a homogeneous dielectric slab. Nonetheless, the shortcoming of this structure is that it supports the very dispersive phononic modes, which in turn limits the acousto-plasmonic coupling.

Plasmon-phonon coupling mechanisms are similar to photon-phonon coupling. The optomechanical part modifies only the form of the particles, and the photoelastic part, acting on the crystal structure of the metal, modifies the dielectric function of the metals. The latter is mainly responsible for observing breathing modes of metal particles in the Raman experiments.[35] However, the photoelastic coupling can be described in metals from a Drude–Lorentz model of dielectric constant: variations in the bulk plasmon frequency are calculated from those of the conduction electron density, while the modulation of the contribution interband is related to local stresses and strain potentials associated with each of the transitions.[8]

A significant amount of work has been conducted to study the strong acoustic vibration of metallic NPs by pump-probe[31] and Raman spectroscopies,[36] leveraging signal amplification near the LSPR mode. The modulation of a plasmon mode by an elastic mode has been studied for a wide set of metal NPs such as spheres,[37] cubes,[38] crosses,[39] cylindrical nanowires,[6] and nanorods.[4] To have an order of magnitude of strain, Soavi *et al.*[4] estimated that the elongation of nanorods 150 nm long is in the order of 5 pm in a typical pump-probe experiment, which gives a strain of 3.3×10^{-5}.

In this work, we propose a new structure that supports plasmonic and elastic modes confined to the NPs for the application of detection in nanosensing technology. Our structure is a glass slab below a periodic system of dielectric Si_3N_4 ribbons supporting gold nanodisks (AuNDs) regularly placed along the ribbons axis. The AuND is characterized by the height hg and the radius R. The dielectric ribbon is characterized by the height H and the width L. The lattice parameter "l" is defined as the distance between two nearest neighboring ribbons (see Fig. 1). We have limited our study to the moving interface contribution.

The outline of our paper is the following: in Sec. II, we put forward the definition of the geometrical parameters of the structure, and we calculate the dispersion and transmission curve of the elastic waves along the ΓX direction. Besides, we demonstrate the existence of WGMs while showing the displacement field of four different modes. The numerical results, including dispersion and transmission curves, are calculated by using the Finite Element (FE) method with the COMSOL Multiphysics FE software. In Sec. III, we calculate the optical transmission spectra with and without the dielectric ribbon and highlight the dipolar nature of the LSPR mode in each AuND. In Sec. IV, we study the coupling between dipolar LSPR mode and four nondispersive elastic WGMs, and then we calculate the modulation of the LSPR wavelength as a function of the acoustic phase of these WGMs. In Sec. V, we summarize and conclude the main results of this work.

TABLE I. Material constants of Au, glass, and Si_3N_4 used in the calculations.

Material	Au	Glass	Si_3N_4
Density (kg/m^3)	19 300	2651	3100
Young modulus (GPa)	78	70	250
Poisson's coefficient	0.44	0.3	0.23

II. ACOUSTICAL PROPERTIES

In this part of the study, the emphasis will be on the phononic aspects and the study of the dispersion curve of the grating. The parameters of the structure are chosen to obtain wide bandgaps, where the localized modes will be excited with the AuNDs. The parameters that we have chosen for the unit cell are the following: for the AuND, a radius of R = 60 nm and a height of hg = 36 nm, for the dielectric ribbon a height of H = 180 nm and a width of L = 210 nm, and for the glass slab a height of h = 60 nm. We apply Bloch-Floquet periodical boundary conditions along the x and y directions of the system. The period is equal to l = 300 nm in the two directions. The z axis is chosen to be perpendicular to the slab and parallel to the AuND axis. The elastic constants for Au, glass, and Si_3N_4 are extracted from Royer and Dieulesaint[40] and are summarized in Table I.

To understand the influence of the ribbons and AuNDs on the dispersion curve of the slab, we performed different band structure computations along the ΓX direction in the first Brillouin zone. We considered single unit cell (see the right picture in Fig. 1), and we applied periodic boundary conditions, using the Bloch-Floquet equations, along the x and y directions.

Figure 2 shows the dispersion curves calculated for the slab (a), slab with ribbon (b), slab with an AuND (c), and slab with a ribbon and an AuND (d) systems. Using the displacement field maps, we can identify three classes of the first-order lamb modes supported by the slab: the longitudinal mode S0 (orange), the horizontal shear mode SH0 (green), and the out of plan slow mode A0 (red) [Fig. 2(a)]. It is well known that the SH0 mode does not interact with the S0 and A0 modes. In the case of slab and ribbon, if we omit the SH0 mode that can be considered the deaf mode

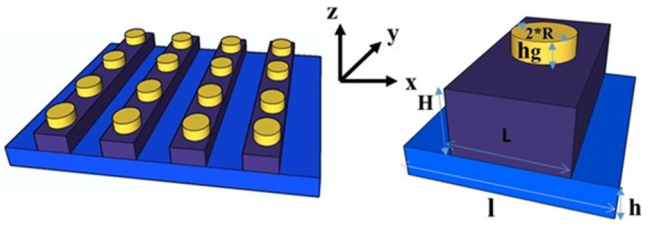

FIG. 1. Sketch of the structure with the unit cell and corresponding geometrical parameters.

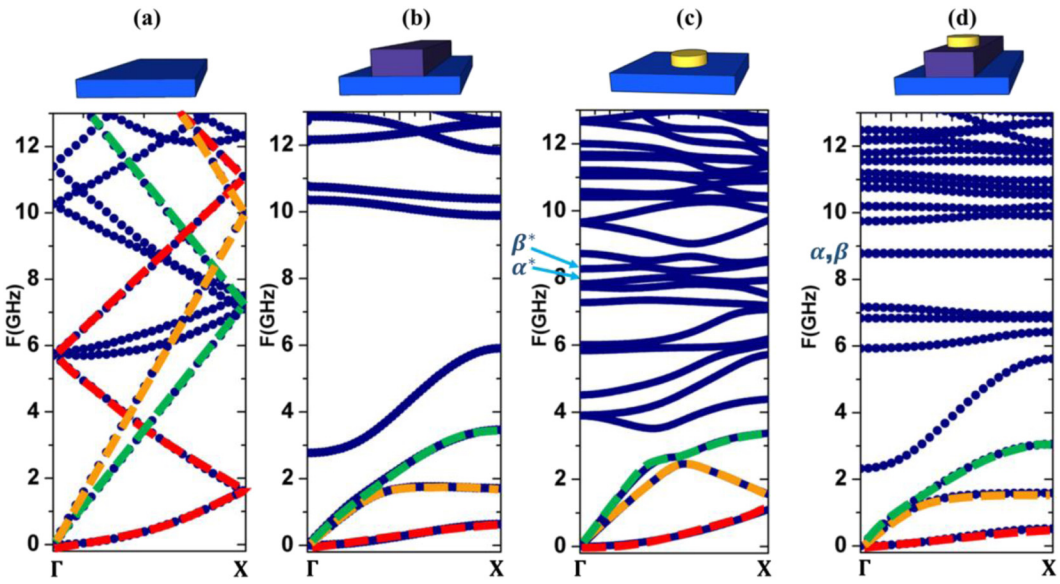

FIG. 2. Dispersion curves along the ΓX direction of the first Brillouin zone: (a) slab, (b) slab with ribbon, (c) slab with an AuND, and (d) slab with a ribbon and an AuND.

[Fig. 2(b)], we obtain the opening of two bandgaps. For the first bandgap, the opening of this gap results from the crossing between A0 and S0 modes. The second two bandgaps are based on the Bragg mechanism. The two branches between 10 GHz and 11 GHz correspond to the flat modes that are completely localized in the glass slab resulting from the contrast of slab toughness.

Figure 2(c) shows the calculated band structure along the ΓX direction of the Brillouin zone. We can observe that all the modes of the slab are shifted to lower frequencies resulting from their mass sensitivity. We can note also the apparition of new branches that correspond to AuND resonance (especially α^* and β^*). These modes are completely mixed with the slab modes and consequently will present leakage of mechanical energy through the slab.

In Fig. 2(d), we present the band structure of slab with ribbon and AuND structure. We can notice that the bandgaps observed for the case of slab with ribbon [Fig. 2(b)] still exist. In the upper part of the band structure, the number of branches increases resulting from their sensitivity to the mass effect, which in turn induces a shift to lower frequencies. The principal point that can be noticed in Fig. 2(d) is the existence of two nearly flat and isolated branches (labeled α and β), especially inside the bandgap situated between 7.2 GHz and 9.7 GHz in Fig. 2(d). The equivalent quadrupolar modes in case of the structure without the ribbon [see Fig. 2(c)] are α^* and β^*, whose respective frequencies are 7.82 GHz and 8.27 GHz at the Γ point. These modes are very dispersive inside the Brillouin zone and do not present any isolated branches. For all these reasons, the introduction of the ribbon is crucial to isolate quasiflat modes and reduce the dispersion of the phononic modes.

For the transmission spectra, we consider a finite system along the x direction containing five unit cells and infinite along the y direction [Fig. 3(a)]. Perfectly Matched Layers (PMLs), which can absorb waves and avoid reflection, are applied on each side of the structure along the finite length direction. We use a mechanical excitation and detection; the incident wave is a S0 Lamb wave of the slab launched by applying a prescribed harmonic acceleration a_x in the (y, z) plane at the left side of the crystal and propagating along the x axis. The transmitted acceleration value is detected and recorded in the far field on the right side of the crystal. The transmission coefficient is normalized to the acceleration field propagating in the homogeneous slab (slab without ribbons and AuNDs).

Figure 3(b) presents the band structure of the phononic crystal given in Fig. 2(d) and compares it with the transmission spectrum through five periods along the y direction. The diagram shows flat branches (labeled α, β, γ, and δ) corresponding to modes confined within the AuND, whose respective frequencies are 8.77 GHz (α), 8.78 GHz (β), 11.55 GHz (γ), and 11.56 GHz (δ). The color map in Fig. 3(c) shows the norm of the displacement vector $\mathbf{u} = (u_x, u_y, u_z)$ at the Γ point. In Fig. 3(c), it shows that the α and β modes are quadrupolar WGMs owing to their displacement field distributions, while modes γ and δ are hexapolar WGMs and are located inside the bandgap between 11.2 GHz and 11.8 GHz. On the transmission spectrum, two peaks appear at 8.77 GHz and 11.55 GHz. Frequencies of those peaks are in agreement with the position to the flat modes labeled α and γ. In the transmission curve, we observe that the SH0 mode (3rd branch) does not contribute to the transmission according to the excitation based on the S0 Lamb mode. The modes β and δ are vibrating along [110] resulting in no coupling to the S0 Lamb wave mode propagating along the x direction. This explains their absence in the transmission spectrum.

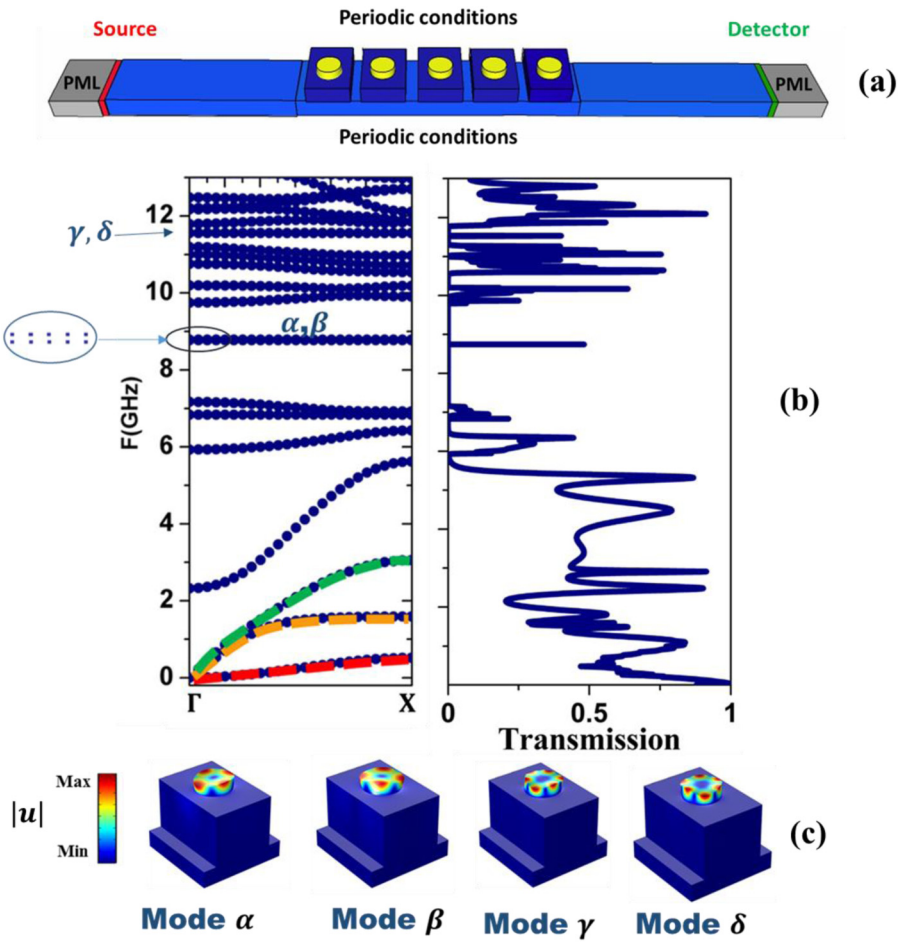

FIG. 3. (a) 3D section of the model adopted for calculating the transmission coefficient of the phononic crystal. (b) Band structure of the phononic crystal of Fig. 2(d) compared with the transmission spectrum though five periods of that system along the direction x. (c) Norm of the displacement field for modes α, β, γ, and δ.

III. PLASMONIC PROPERTIES

In this section, we are in a position to discuss the optical proprieties of the used materials. The glass slab has a refractive index $n_s = 1.5$ and the one of the dielectric ribbon Si_3N_4 is $n_r = 2$. The choice of these two materials can be explained by three main factors. Firstly, glass and Si_3N_4 are two abundant materials extremely used in plasmonics device industries. Thus, their fabrication technologies are in an advanced stage. Secondly, since the extraordinary and ordinary index values are very close together, the glass anisotropy does not affect the plasmonic response. At last, the two over mentioned dielectric materials are not absorbent in the visible spectrum. In order to describe gold's permittivity in the visible spectrum, we use the Drude–Lorentz model, which is given by the following formula:

$$\varepsilon(\omega) = \varepsilon_\infty + \sum_{m=0}^{M} \frac{f_m \omega_p^2}{\omega_m^2 - \omega^2 + i\omega\Gamma_m}$$

where ε_∞ is the relative permittivity at infinite frequency, ω_p is the plasma frequency, and ω_m, f_m, and Γ_m are the resonance frequency, the strength, and the damping of the mth oscillator, respectively. We use $M = 5$ damped harmonic oscillators in order to take the interband transitions of gold into account. The values, taken from Palik,[41] are listed in Table II.

Figure 4 shows the transmission spectra of our structure with the AuND but with and without the ribbon. We excite our structure with an electric field in normal incidence (propagation along the z axis, from below the glass slab) on the AuND, polarized along the y direction to excite the surface plasmon mode. The black curve

TABLE II. Values of the parameters of the Drude–Lorentz model describing the gold dielectric constant in our FE code.

Oscillator m	f_m	ω_p(rad s^{-1})	ω_m(rad s^{-1})	Γ_m(rad s^{-1})
0	0.76	$1.371\,88 \times 10^{16}$	0	$8.052\,02 \times 10^{13}$
1	0.024	$1.371\,88 \times 10^{16}$	$6.304\,88 \times 10^{14}$	$3.661\,39 \times 10^{14}$
2	0.01	$1.371\,88 \times 10^{16}$	$1.260\,98 \times 10^{15}$	$5.241\,41 \times 10^{14}$
3	0.71	$1.371\,88 \times 10^{16}$	$4.510\,65 \times 10^{15}$	$1.321\,75 \times 10^{15}$
4	0.601	$1.371\,88 \times 10^{16}$	$6.538\,85 \times 10^{15}$	$3.789\,01 \times 10^{15}$
5	4.384	$1.371\,88 \times 10^{16}$	$2.023\,64 \times 10^{16}$	$3.363\,62 \times 10^{15}$

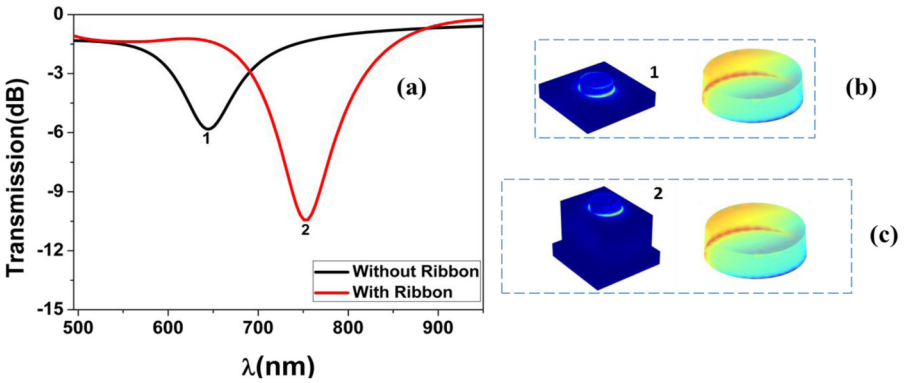

FIG. 4. (a) Transmission spectra through the structure with and without the presence of the dielectric ribbon. The four electric field maps represent modes 1 and 2 found together with the representation of their surface charge distribution.

(labeled 1) gives us only one dipolar plasmonic mode, whose electric field is confined close to the slab at the bottom of the AuND. The resonance wavelength of this mode is $\lambda = 645$ nm.

The mode corresponding to the peak labeled 2 on the red curve with a wavelength of 753 nm is the same localized plasmon as mode 1, but it shifts toward longer wavelength by about 100 nm. This shift is because the ribbon has a refractive index that is higher than that of the glass slab, which is consistent with other theories and experiments in this field.[13]

IV. ACOUSTO-PLASMONIC MODULATION

We investigate now the modulation of the resonance wavelength of the plasmonic dipolar mode under elastic deformation during an acoustic period, through the moving interface mechanism: the elastic wave travels through the system and during that process it deforms the interface between two different materials. In fact, within a thin layer in the vicinity of the interface whose thickness is proportional to the displacement field normal to the interface, a switch in the material occurs where the volume occupied by material 1 becomes occupied by material 2 and vice versa. This process leads to a time-varying modification of the dielectric constant, which then affects the optical waves. The deformation is applied on a whole structure, and the moving interface mechanism is then proportional to the displacement field and to the difference between the dielectric constants of the materials on both sides of the interface.

The deformation is computed for an eigenmode of the mechanical system by imposing a maximal displacement equal to 2% of the radius of the AuND ($u_{\max} = 1.6$ nm). It should be noted that the maximum sound deformation imposed is in the order of 2%, which is unrealistic at the crystalline scale. However, the values we obtained numerically can be scaled to a more realistic case. It results in the time-varying shift of the wavelength of the plasmonic mode in the transmission spectrum, whose amplitude depends on the acoustic phase $\phi = 2\pi Ft$, where F is the eigenfrequency of the considered acoustic mode and t is the time. Let us mention that we have chosen the origin of the phase $\phi = 0$ such that the AuND is undeformed for this value. In the following, we present the influence of the four previously identified phononic modes (α, β, γ, and δ) on the optical properties of our system.

Figure 5 presents the modulation of the transmission spectra under deformation by the two elastic modes α and β for different acoustic phases. The quadrupole mode (α) (8.77 GHz) introduces notable modifications in the LSPR wavelength around its value at rest $\lambda_{ref} = 753$ nm, as shown in Fig. 5(a), while for the quadrupolar mode β (8.78 GHz), the LSPR wavelength modulation is smaller [Fig. 5(b)]. The same calculations done with the high-frequency modes (γ: $F = 11.55$ GHz, δ: $F = 11.56$ GHz) show no modification in the transmission spectra. Figure 5(c) displays the displacement field distribution (color map corresponds to the norm of $|\mathbf{u}|$) of the 4 elastic WGMs and the red arrows indicate the displacement itself (red arrows represents the real part of $\mathbf{u}$). To better comprehend the contribution of the multipolar modes in the acousto-plasmonic coupling, we elucidate it with an analytical model. Concerning the AuNDs, the equation of the wave is written as follows:

$$\Delta_{\parallel} E_z(r, \varphi) - \xi^2 E_z(r, \varphi) = 0.$$

The solution of the above equation in polar coordinates (r, φ) are of the following form:

$$E_z = E_0 \cos(n\varphi) J_n(\xi r),$$

where E_0 is the wave amplitude, n is a positive integer, and J_n is the Bessel function of the order n. Since the dipolar plasmonic mode induces a strong exaltation of the intensity of the electric field on the edges of the AuND, a boundary condition has to be applied at the edge of the AuND at $r = R$,

$$J_n'(\xi R) = 0.$$

We ultimately get the following expression:

$$E_r(r, \varphi) = E_0 \cos(n\varphi) J_n(x'_n r/R),$$

with $\xi = \frac{x'_n}{R}$ dispersion equation and the coefficients x'_n representing the zeros of the derivative of the Bessel functions. The phononic modes are multipolar deformation, in which the radius of the cavity oscillates periodically as a function of φ,

$$R(\varphi) = R_0 + \delta R \cos(m\varphi), \qquad m \neq 0,$$

with R_0 being the radius of the AuND at rest. To evaluate how the LSPR dipolar mode is modified following the deformation of the

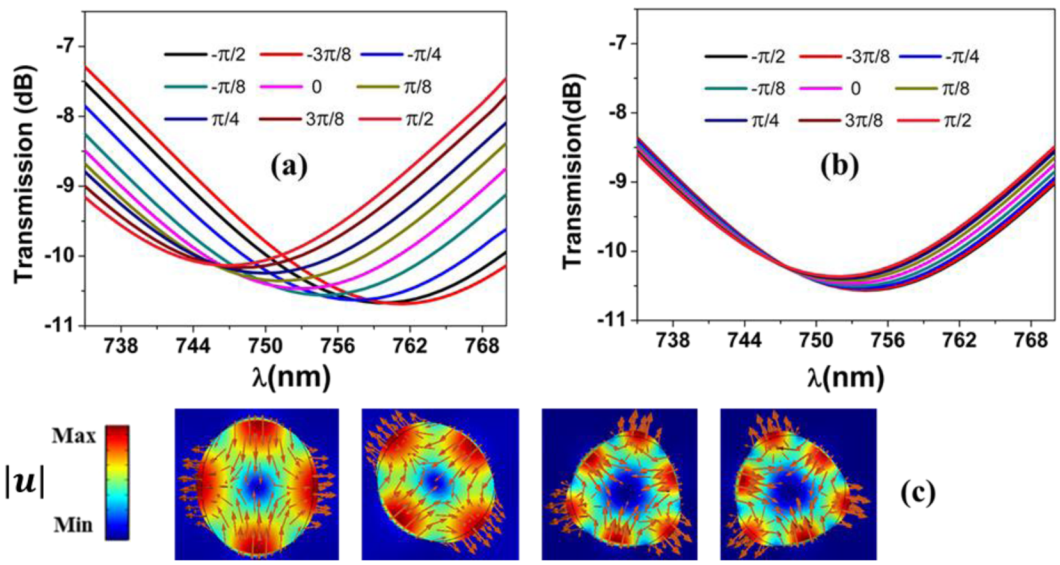

FIG. 5. Evolution of the transmission spectra for different values of the elastic phase for the two elastic modes: (a) mode α and (b) mode β. (c) Norm of the displacement field distribution [$\mathbf{u} = (u_x,\ u_y,\ u_z)$] for α, β, γ, and δ modes at the Γ point (color map shows the norm of displacement field $|\mathbf{u}|$; red arrows represents the real part of $\mathbf{u}$).

radius of the AuND, we develop the electric field of this mode in the form of a linear combination of the solutions of the wave equation in cylindrical coordinates. The electric field can be developed as a linear combination of the solution functions of the wave equation in (r, φ, z) coordinates:

$$[E_z(r,\varphi)] = \sum_{n=0}^{\infty} a_n \cos(n\varphi) J_n(\xi r).$$

With $a_N \approx 1$ and $a_n \ll 1$, $n \neq N$. The new boundary condition at the limits can be written as follows:

$$[E_z]^l(R(\varphi),\varphi) = \sum_{n=0}^{\infty} a_n \cos(n\varphi) J_n[\xi(R_0 + \delta R\cos(m\varphi))] = 0.$$

Since the amplitude deformation is weak, the ξR_0 value remains close to x'_p and can be written as $\xi R_0 = x'_n(1+\eta)$. To the first-order a_n, ε *et* $\delta R/R_0$ along with $J'_N(x'_N) = 0$,

$$J''_N(x'_n)\left\{\cos(N\varphi)\eta + \frac{\delta R}{2R_0}[\cos((m-N)\varphi) + \cos((m+N)\varphi)]\right\} + \sum_{n\neq N} a_n \cos(n\varphi) J'_n(x'_n) = 0.$$

The unique impact of this deformation is the modulation of the resonance wavelength of the LSPR dipolar mode. Nonetheless, m and η are different from zero only if $N = m - N$, and this only happens if m is even ($m = 2$). In this case, the only modes affected by the phononic deformation are for $N = m/2$, while for the noncoupled modes, m is odd (m = 3) and we have

$$\eta_N = \frac{\delta R}{2R_0} x'_N,$$

$$a_N = 1,$$

$$a_{3N} = \frac{\delta R}{2R_0}\frac{J''_N(x'_N)}{J''_{3N}(x'_N)},$$

$$a_N = 0,\ n \neq N,\ 3N.$$

Therefore, $\begin{cases} R(\varphi) = R_0 + \delta R\cos(2\varphi) & \text{for } m = 2, \\ R(\varphi) = R_0 & \text{for } m = 3. \end{cases}$

For hexapolar modes $m = 3$, the displacement of a half acoustic period generates a phase opposition, which results in a zero acousto-plasmonic modulation. However, the displacement of the acoustic quadrupole modes $m = 2$ is in phase, which in turn leads to a strong acousto-plasmonic coupling. On the other hand, this fact can be understood through considerations about the respective symmetries of those elastic modes and the LSPR dipolar mode. The α mode oscillates according to the periodicity of the AuNDs, while the β mode oscillates in the [110] direction to the periodicity of the AuNDs. The first elastic mode α moves essentially along the principal axes of the array (Ox and Oy), and the charge distribution of LSPR mode is antisymmetric with respect to the zx plane and symmetrical to the zy plane. These two symmetries couple perfectly, and a strong acousto-plasmonic coupling allows us to induce a significant shift around λ_{ref}. At 8.78 GHz (β), the displacement fields undergo a rotation of $\pi/4$ compared to the (α) mode, which

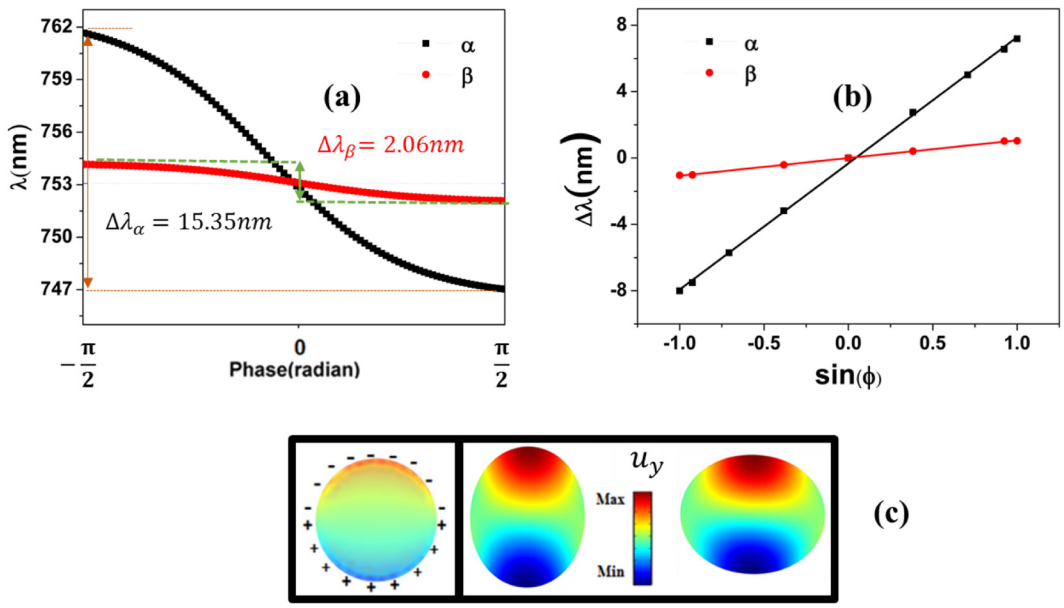

FIG. 6. (a) Wavelength modulation of the plasmonic dipolar mode by each of the two quadrupolar elastic modes α and β. (b) Evolution of the LSPR wavelength as a function of the sinus of the acoustic phase for each of the four elastic modes. (c) Left: distribution of the surface charges of the LSPR dipolar mode; right: y component of the displacement field for the quadrupolar mode α and phases $\phi = -\pi/2$ (left) and $\phi = -\pi/2$ (right).

breaks the symmetry with the principal axes and does not favor the coupling with the dipolar mode since it couples only with projections of the displacements fields following the x and y directions. This allows us to explain the weak modification around λ_{ref}.

In Fig. 6(a), the resonance wavelength of the dipolar LSPR undergoes sinusoidal modulation around the average value of 753 nm for the quadrupolar WGMs (α, β) due to the moving interface during one elastic period. The corresponding modulation

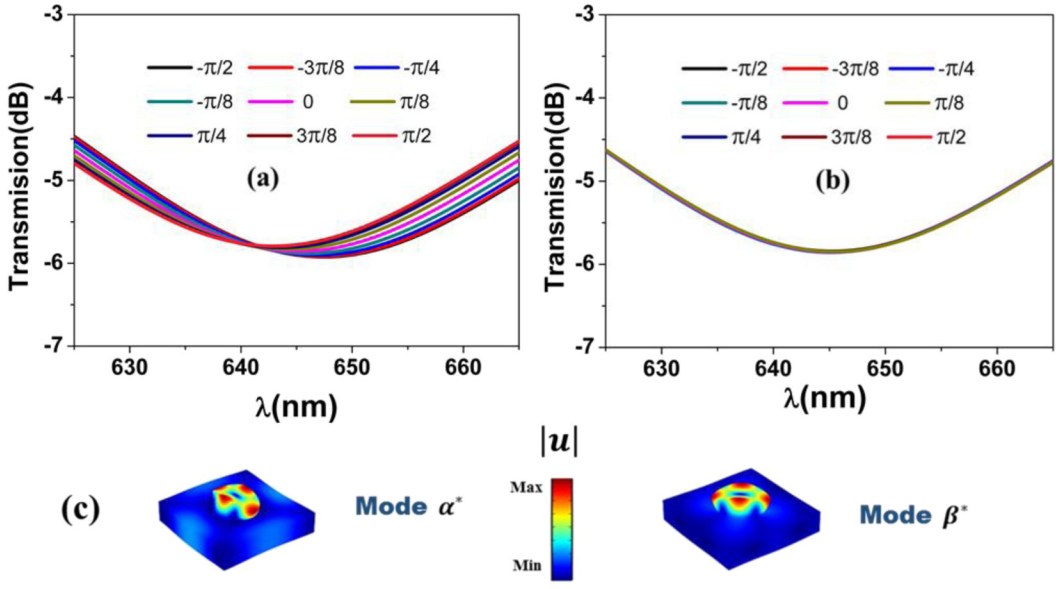

FIG. 7. (a) Wavelength modulation of the dipolar LSPR mode of the two quadrupolar elastic modes: (a) mode α^* and (b) mode β^*. (c) Norm of the displacement field distribution for α^* and β^* modes at the Γ point.

amplitude are $\Delta\lambda_\alpha = 15.35$ nm and $\Delta\lambda_\beta = 2.06$ nm. No wavelength modulation has been obtained with hexapolar modes γ and δ, and then the corresponding slope is equal to zero. A clearer representation shows in Fig. 6(b) the evolution of the resonance wavelength of the LSPR mode as a function of the sine of the phase of the WGMs, under interaction with the two quadrupole modes α and β. We have utilized a linear fit to represent this curve [Fig. 6(b)]. Notice that the fitting errors are very weak, and the error bars are not noticeable in the curve; therefore, they were not shown. We notice that the wavelength depends linearly on the sine of the phase, so that we can write $\Delta\lambda = \mathrm{p}\sin(\phi)$ where the parameter p is the slope. This approximation stays valid because of the weak gap of the points relative to the linear fit. The α mode, with the lowest frequency (8.77 GHz), is the most sensitive to the deformation with a slope equal to $\Delta\lambda/\sin(\phi) = 7.64$ nm. The enhanced sensitivity of the (α) mode is since the y component of the displacement fields is coupled to the dipolar LSPR mode and has the same symmetry along the x axis. Besides, the maximum of the displacement field coincides with the symmetry of the dipolar mode. The y component of the quadrupolar elastic mode vibrates according to the dipolar symmetry of the plasmonic mode; this will affect the charge distribution in the vicinity of the interface of the AuNDs, which will increase the acoustic-plasmonic sensitivity.

To draw an analogy between the structure with and without the ribbon, Fig. 7 presents the modulation of the transmission spectra under deformation by the two elastic modes $\alpha^\star$ and $\beta^\star$ for different acoustic phases. The $\alpha^\star$ mode (7.82 GHz) introduces notable modifications of the LSPR wavelength around its value at rest $\lambda_{ref} = 645$ nm [Fig. 7(a)]. We note a low sensitivity of the $\alpha^\star$ mode compared to the α mode in the presence of the ribbon. The same calculations are done with the $\beta^\star$ mode (8.27 GHz), which presents a very weak coupling with the dipolar LSPR mode [Fig. 7(b)]. This coupling is very weak compared to the β mode (this mode is calculated with the presence of the ribbon). Figure 7(c) illustrates the dispersive nature of the $\alpha^\star$ and $\beta^\star$ modes inside the slab. The figure shows the existence of interactions between $\alpha^\star$ and $\beta^\star$ modes and the Lamb modes of the slab [see Fig. 2(c)], which make the displacement of one part of the elastic energy of $\alpha^\star$ and $\beta^\star$ WGMs in the slab. To quantify the role of the added ribbon between the slab and the AuND, we have calculated the sensitivity values of all modes and have summarized them in Table III.

To compare our results with those of the literature, we divided the sensitivity by the maximum displacement $u_{\max} = 1.6$ nm. The numerical results obtained show that the interaction between the LSPR mode and the elastic quadrupole mode α is almost 7.68 times more sensitive than in an AuND deposited directly on a slab. The orders of magnitude of these values are in agreement with those obtained in the literature for equivalent systems.[2,6] The addition of the ribbon, on the one hand, allowed the confinement of the quadrupolar modes, and, on the other hand, it allowed the isolation of the modes. In a nutshell, it can be concluded that the best confinement of the phononic modes gives good acousto-plasmonic coupling.

TABLE III. Comparison table in sensitivity between different WGMs.

	Plasmonic λ_{LSPR} (nm)	
Phononic F (GHz)	$\Delta\lambda_{\alpha,\beta}$ (nm)	$\Delta\lambda/u_{\max}\sin(\phi)$
WGM (α), $F = 8.77$	15.35	9.60
WGM (β), $F = 8.78$	2.07	1.30
WGM ($\alpha^\star$), $F = 7.82$	2.01	1.25
WGM ($\beta^\star$), $F = 8.27$	0.26	0.16

V. CONCLUSION

We have numerically studied the plasmonic and elastic response of AuNDs deposited on dielectric ribbons of Si_3N_4 lying on a glass slab. It was pointed out from the optical and elastic transmission curves that this structure supports localized modes of different natures: dipolar LSPR for plasmonic and WGMs for acoustic modes; they are both very confined in the AuNDs. The calculated phononic dispersion and transmission curves showed the appearance of elastic flat modes (WGMs); the latter are not dispersive and have an excellent intrinsic quality factor. We then observed that the symmetry of displacement as well as the nature of WGMs and deformation, significantly, affect the plasmonic response up to $\Delta\lambda = 15.35$ nm for a maximal deformation of 1.6 nm and for the phononic quadrupolar mode, which shows that the coupling is very high compared to that found in optomechanical cavities. This study shows that the optimization of the geometry of a metallic nanostructure makes it possible to reach very high acousto-plasmonic coupling sensitivities. However, it appears that this improvement is made with strong confined phononic modes in the AuNDs. It is found that without ribbons, the optomechanical coupling decreases. The result presented in this paper is actually more general and may appear as a bounding limit of acousto-plasmonic biosensors. We believe that this new structure studied in this work is promising to understand even more the interaction of plasmon-phonon nanostructures, which are well known for sensing applications, and that it could pave the way for new devices in the future that take both the elastic appearance and plasmonic to the nanoscale.

ACKNOWLEDGMENTS

A. Akjouj gratefully acknowledges the hospitality of the Faculty of Science, University of Moulay Ismail of Meknes. This work was partially supported by the program FINCOME "Centre National pour la Recherche Scientifique et Technique, Morocco."

REFERENCES

[1]J.-W. Kim, O. Kovalenko, Y. Liu, and J.-Y. Bigot, "Exploring the Angstrom excursion of Au nanoparticles excited away from a metal surface by an impulsive acoustic perturbation," ACS Nano **10**, 10880–10886 (2016).
[2]A. Mrabti, G. Lévêque, A. Akjouj, Y. Pennec, B. Djafari-Rouhani, R. Nicolas, T. Maurer, and P.-M. Adam, "Elastoplasmonic interaction in metal-insulator-metal localized surface plasmon systems," Phys. Rev. B **94**, 075405 (2016).
[3]B. Dong, X. Chen, F. Zhou, C. Wang, H. F. Zhang, and C. Sun, "Gigahertz all-optical modulation using reconfigurable nanophotonic metamolecules," Nano Lett. **16**, 7690–7695 (2016).
[4]G. Soavi *et al.*, "Ultrasensitive characterization of mechanical oscillations and plasmon energy shift in gold nanorods," ACS Nano **10**, 2251–2258 (2016).
[5]R. Thijssen, E. Verhagen, T. J. Kippenberg, and A. Polman, "Plasmon nanomechanical coupling for nanoscale transduction," Nano Lett. **13**, 3293–3297 (2013).

[6]S. El-Jallal, A. Mrabti, G. Lévêque, A. Akjouj, Y. Pennec, and B. Djafari-Rouhani, "Phonon interaction with coupled photonic-plasmonic modes in a phoxonic cavity," AIP Adv. **6**, 122001 (2016).
[7]S.-C. Yang *et al.*, "Enhanced detection sensitivity of higher-order vibrational modes of gold nanodisks on top of a GaN nanorod array through localized surface plasmons," Appl. Phys. Lett. **105**, 211103 (2014).
[8]A. Ahmed, M. Pelton, and J. R. Guest, "Understanding how acoustic vibrations modulate the optical response of plasmonic metal nanoparticles," ACS Nano **11**, 9360–9369 (2017).
[9]R. Chikkaraddy *et al.*, "How ultranarrow gap symmetries control plasmonic nanocavity modes: From cubes to spheres in the nanoparticle-on-mirror," ACS Photonics **4**, 469–475 (2017).
[10]Z. Oumekloul, S. Lahlali, A. Mir, and A. Akjouj, "Evolution of LSPR of gold nanowire chain embedded in dielectric multilayers," Opt. Mater. **86**, 343–351 (2018).
[11]E. Galopin, J. Niedziółka-Jönsson, A. Akjouj, Y. Pennec, B. Djafari-Rouhani, A. Noual, R. Boukherroub, and S. Szunerits, "Sensitivity of plasmonic nanostructures coated with thin oxide films for refractive index sensing: Experimental and theoretical investigations," J. Phys. Chem. C **114**, 11769–11775 (2010).
[12]S. Szunerits, S. Ghodbane, J. Niedziółka-Jönsson, E. Galopin, F. Klauser, A. Akjouj, Y. Pennec, B. Djafari-Rouhani, R. Boukherroub, and D. Steinmuller, "Development and characterization of a diamond-based localized surface plasmon resonance interface," J. Phys. Chem. C **114**, 3346–3353 (2010).
[13]A. Akjouj *et al.*, "Nanometal plasmonpolaritons," Surf. Sci. Rep. **68**, 1–67 (2013).
[14]W. A. Murray, B. Auguié, and W. L. Barnes, "Sensitivity of localized surface plasmon resonances to bulk and local changes in the optical environment," J. Phys. Chem. C **113**, 5120–5125 (2009).
[15]D. R. Raj, S. Prasanth, and C. Sudarsanakumar, "Development of LSPR-based optical fiber dopamine sensor using L-tyrosine-capped silver nanoparticles and its nonlinear optical properties," Plasmonics **12**, 1227–1234 (2017).
[16]Y.-L. Ho, L.-C. Huang, E. Lebrasseur, Y. Mita, and J.-J. Delaunay, "Independent light-trapping cavity for ultra-sensitive plasmonic sensing," Appl. Phys. Lett. **105**, 061112 (2014).
[17]A. D. McFarland, M. A. Young, J. A. Dieringer, and R. P. Van Duyne, "Wavelength-scanned surface-enhanced Raman excitation spectroscopy," J. Phys. Chem. B **109**, 11279–11285 (2005).
[18]G. K. Pandey, N. K. Pathak, R. Uma, and R. P. Sharma, "Study of surface-enhanced Raman scattering of plasmonic coupled biomolecule: Role of multi-layered nanosphere," Plasmonics **13**, 221–229 (2018).
[19]J.-M. Nam, J.-W. Oh, H. Lee, and Y. D. Suh, "Plasmonic nanogap-enhanced Raman scattering with nanoparticles," Acc. Chem. Res. **49**, 2746–2755 (2016).
[20]S. Pillai, F. J. Beck, K. R. Catchpole, Z. Ouyang, and M. A. Green, "The effect of dielectric spacer thickness on surface plasmon enhanced solar cells for front and rear side depositions," J. Appl. Phys. **109**, 073105 (2011).
[21]K. N'Konou, L. Peres, and P. Torchio, "Optical absorption modeling of plasmonic organic solar cells embedding silica-coated silver nanospheres," Plasmonics **13**, 297–303 (2018).
[22]K. R. Catchpole and A. Polman, "Design principles for particle plasmon enhanced solar cells," Appl. Phys. Lett. **93**, 191113 (2008).
[23]S. Pillai, C. E. Disney, Y. Yang, and M. A. Green, "The effect of ageing on the scattering properties of silver nanoparticles for a plasmonic solar cell," J. Appl. Phys. **118**, 153102 (2015).
[24]X. Yi *et al.*, "Polarization-dependent detection of cylinder nanoparticles with mode splitting in a high-Q whispering-gallery microresonator," Appl. Phys. Lett. **97**, 203705 (2010).
[25]V. Juvé *et al.*, "Probing elasticity at the nanoscale: Terahertz acoustic vibration of small metal nanoparticles," Nano Lett. **10**, 1853–1858 (2010).
[26]B. Sturman and I. Breunig, "Acoustic whispering gallery modes within the theory of elasticity," J. Appl. Phys. **118**, 013102 (2015).
[27]Y. Jin *et al.*, "Tunable waveguide and cavity in a phononic crystal plate by controlling whispering-gallery modes in hollow pillars," Phys. Rev. B **93**, 054109 (2016).
[28]Y. Pennec, B. Djafari-Rouhani, H. Larabi, A. Akjouj, and G. Lévêque, "Perpendicular transmission of acoustic waves between two substrates connected by sub-wavelength pillars," New J. Phys. **14**, 073039 (2012).
[29]S. Hemon, A. Akjouj, A. Soltani, Y. Pennec, Y. El Hassouani, A. Talbi, and B. Djafari Rouhani, "Hypersonic band gap in an AlN/TiN bilayer phononic crystal slab," Appl. Phys. Lett. **104**, 063101 (2014).
[30]J. Margueritat, J. Gonzalo, C. N. Afonso, A. Mlayah, D. B. Murray, and L. Saviot, "Surface plasmons and vibrations of self-assembled silver nanocolumns," Nano Lett. **6**, 2037–2042 (2006).
[31]A. Crut, P. Maioli, N. Del Fatti, and F. Vallée, "Acoustic vibrations of metal nano-objects: Time-domain investigations," Phys. Rep. **549**, 1–43 (2015).
[32]Y. Shao, X. Li, L. Wu, and D. Wang, "Cu diffusion in CdTe detected by nano-metal-plasmonic enhanced resonant Raman scattering," J. Appl. Phys. **125**, 013101 (2019).
[33]B. Dacosta Fernandes *et al.*, "Acoustic vibrations of Au nano-bipyramids and their modification under Ag deposition: A perspective for the development of nanobalances," ACS Nano **7**, 7630–7639 (2013).
[34]E. Duval, A. Boukenter, and B. Champagnon, "Vibration eigenmodes and size of microcrystallites in glass: Observation by very-low-frequency Raman scattering," Phys. Rev. Lett. **56**, 2052–2055 (1986).
[35]G. Bachelier and A. Mlayah, "Surface plasmon mediated Raman scattering in metal nanoparticles," Phys. Rev. B **69**, 205408 (2004).
[36]N. Large *et al.*, "Acousto-plasmonic hot spots in metallic nano-objects," Nano Lett. **9**, 3732–3738 (2009).
[37]M. A. van Dijk, M. Lippitz, and M. Orrit, "Detection of acoustic oscillations of single gold nanospheres by time-resolved interferometry," Phys. Rev. Lett. **95**, 267406 (2005).
[38]H. Petrova *et al.*, "Time-resolved spectroscopy of silver nanocubes: Observation and assignment of coherently excited vibrational modes," J Chem. Phys. **126**, 094709 (2007).
[39]K. O'Brien, N. D. Lanzillotti-Kimura, J. Rho, H. Suchowski, X. Yin, and X. Zhang, "Ultrafast acousto-plasmonic control and sensing in complex nanostructures," Nat. Commun. **5**, 4042 (2014).
[40]D. Royer and E. Dieulesaint, *Elastic Waves in Solids I: Free and Guided Propagation* (Springer-Verlag, Berlin, 2000).
[41]E. D. Palik, *Handbook of Optical Constants of Solids* (Naval Research Laboratory, Washington, DC, 2012).